Inhibition of tumor growth and metastasis by a self-therapeutic nanoparticle

Rochelle R. Arvizo[a], Sounik Saha[a], Enfeng Wang[a], J. David Robertson[b], Resham Bhattacharya[a], and Priyabrata Mukherjee[a,c,d,1]

[a]Department of Biochemistry and Molecular Biology, [c]Department of Physiology and Biomedical Engineering, and [d]Mayo Clinic Cancer Center, Mayo Clinic College of Medicine, Rochester, MN 55905; and [b]Department of Chemistry and University of Missouri Research Reactor, University of Missouri, Columbia, MO 65211

Edited by Chad A. Mirkin, Northwestern University, Evanston, IL, and approved March 12, 2013 (received for review August 21, 2012)

Although biomedical applications of nanotechnology, which typically involve functionalized nanoparticles, have taken significant strides, biological characterization of unmodified nanoparticles remains underinvestigated. Herein we demonstrate that unmodified gold nanoparticles (AuNPs) inhibit the proliferation of cancer cells in a size- and concentration-dependent manner by abrogating MAPK-signaling. In addition, these AuNPs reverse epithelial-mesenchymal transition (EMT) in cancer cells by reducing secretion of a number of proteins involved in EMT, up-regulating E-Cadherin, and down-regulating Snail, N-Cadherin, and Vimentin. Inhibition of MAPK signaling and reversal of EMT upon AuNP treatment inhibits tumor growth and metastasis in two separate orthotopic models of ovarian cancer. Western blot analyses of tumor tissues reveal up-regulation of E-Cadherin and down-regulation of Snail and phospho-MAPK, confirming the reversal of EMT and inhibition of MAPK signaling upon AuNP treatment. The ability of a single self-therapeutic nanoparticle to abrogate signaling cascades of multiple growth factors is distinctive and purports possible medical applications as potential antitumor and antimetastatic agent.

drug delivery | heparin-binding growth factors

Major efforts in biomedical nanotechnology have concentrated in the area of drug delivery and biosensor applications. Although size- and shape-dependent physico-chemical and opto-electronic properties of inorganic nanoparticles have been studied in detail (1), their biological properties remain to be elucidated. Gold nanoparticles (AuNPs), in particular, have attracted wide attention in various biomedical applications because they are biocompatible, easy to synthesize, characterize, and surface modify due to the strong ability of AuNPs to bind to –SH- and $–NH_2$-containing molecules (2). Thus, biological molecules, particularly proteins, can serve as important substrates in binding to AuNP through cysteine and lysine residues. The preferential binding of cysteine/lysine-rich proteins to AuNP may then alter their structure and biological functions, allowing AuNPs to be exploited as a therapeutic agent. We recently demonstrated that AuNPs upon binding HB–GFs (Heparin-binding growth factors) such as vascular endothelial GF 165 (VEGF165) and basic fibroblast GF (bFGF) inhibited their function due to the unfolding of the protein structure (3). Since HB–GFs are critically important for angiogenesis and epithelial–mesenchymal transition (EMT), a mechanism that confers metastatic potential to tumor cells, AuNPs may find wide applications as therapeutic agents in angiogenesis-dependent disorders and in preventing tumor growth and metastasis in cancer (4).

Epithelial ovarian cancer (EOC) is one of the deadliest among gynecologic malignancies (5). Despite optimal surgical debulking and carefully designed chemotherapeutic regimen, relapse is almost inevitable with a more aggressive drug-resistant phenotype and metastatic spread (6). EMT is one of the main mechanisms underlying development of cancer metastasis, which induces stem-like properties and confers drug resistance to tumor cells (7, 8). Thus, reversing the process of EMT could potentially be a unique therapeutic approach to sensitize drug-resistant cells to chemotherapeutics and to inhibit metastasis. Repression of E-Cadherin (E-Cad) is the hallmark of EMT and occurs through transcriptional repressors such as Vimentin, Snail, Slug, Twist, etc. (8–10). Down-regulation of E-Cad expression by its transcriptional repressors through several compensatory and independent mechanisms poses a challenge for anti-EMT therapy (11–13). Since AuNPs can inhibit the function of a multitude of HB–GFs responsible for EMT (3, 14, 15), it can potentially act as a multifunctional molecule to reverse epithelial plasticity, thereby inhibiting tumor growth and metastasis. A number of inflammatory GFs containing the HB domain are pivotal in regulating EMT such as VEGF165, HB–EGF, bFGF, TGF-β, TNF-α, etc., which are overexpressed in ovarian cancer and other solid tumors (16). In clinical samples, high levels of these HB–GFs correlate with advanced stage of the disease, increased metastasis, and poor survival (17). Thus, ovarian cancer represents an important model to test the self-therapeutic anti-EMT and antitumor property of AuNPs.

Results

AuNPs Inhibit the Proliferation of Ovarian Cancer Cells in a Size-Dependent Manner. AuNPs synthesized by the citrate reduction method without any further modification were used for all of the studies and are referred to as unmodified nanoparticles in this paper. To determine a relationship between the size and the biological function of the nanoparticles, we used AuNPs of four different sizes (circa 5, 20, 50, or 100 nm) and characterized them by transmission electron microscopy (TEM), dynamic light scattering (DLS) and zeta potential measurements (Figs. S1 and S2). Next we sought to determine the effect of these AuNPs on the proliferation of three different ovarian cancer cell lines—A2780, OVCAR5, and SKOV3-ip cells—and compare them with normal ovarian surface epithelial (OSE) (18) cells. Our findings demonstrated that both size and concentration of AuNPs play a pivotal role in inhibiting the proliferation of ovarian cancer cells (as determined by ^{3}[H]-Thymidine incorporation), in a time-dependent manner (Fig. 1 and Fig. S3). While 20 nm AuNPs exhibited the highest efficacy at 72 h in inhibiting the proliferation of SKOV3-ip cells, AuNPs of 5 nm showed only a modest inhibition, whereas no inhibition was observed with AuNPs of 50 and 100 nm size (Fig. 1). Furthermore, the proliferation of normal OSE cells was not affected (Fig. S4*A*). AuNPs exhibited similar size and concentration-dependent effects on A2780 and OVCAR5 cells (Fig. S3). These results clearly demonstrate that the inhibitory effect of AuNPs is dependent on surface size, with 20 nm AuNPs showing the greatest efficacy. Since our working hypothesis is that secreted GFs from malignant cells are inhibited by AuNPs, most of our experiments are performed under starving conditions. However, it is important to test the efficacy

Author contributions: R.R.A, R.B. and P.M. designed research; R.R.A., S.S., E.W., and J.D.R. performed research; R.R.A. and J.D.R. contributed new reagents/analytic tools; R.R.A., S.S., E.W., J.D.R., R.B., and P.M. analyzed data; and R.R.A., S.S., R.B., and P.M. wrote the paper.

The authors declare no conflict of interest.

This article is a PNAS Direct Submission.

[1]To whom correspondence should be addressed. E-mail: mukherjee.priyabrata@mayo.edu.

This article contains supporting information online at www.pnas.org/lookup/suppl/doi:10.1073/pnas.1214547110/-/DCSupplemental.

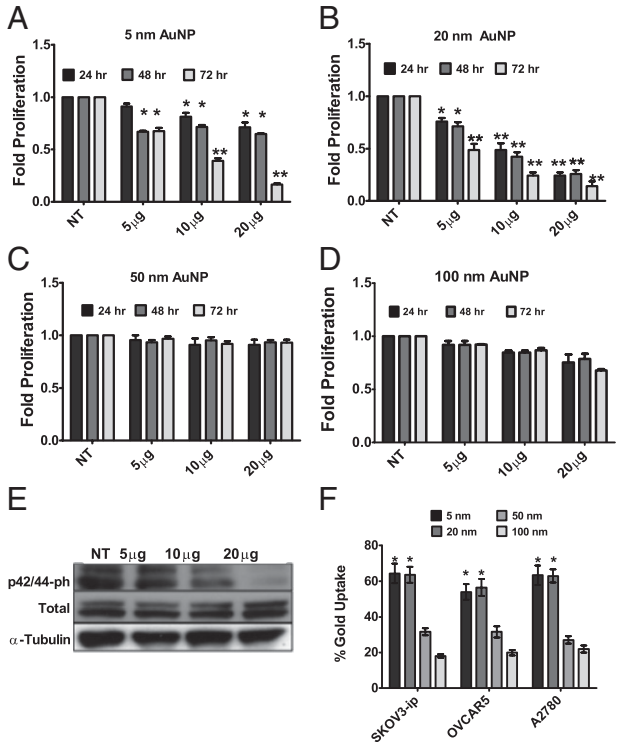

Fig. 1. Inhibition of cellular proliferation, downstream signaling, and uptake is dependent on the size of AuNPs. Serum-starved A2780 cells were incubated with (*A*) 5 nm, (*B*) 20 nm, (*C*) 50 nm, or (*D*) 100 nm AuNPs for either 24, 48, or 72 h. [^{3}H]Thymidine incorporation is represented as fold proliferation. (*E*) Serum-starved SKOV3-ip was incubated with 20 nm AuNPs (different concentrations) for 48 h, and 20 μg of cell lysates were immunoblotted with antibodies to p42/44-phospho (p42/44-ph) and total p42/44 (Total) levels in the cell extracts. α-Tubulin was used as a loading control. (*F*) Cellular uptake of AuNPs into cells. The uptake was determined by measuring the gold concentration in cells using INAA. The *y* axis represents gold concentrations as percentage of microgram of total dry mass of cells. Values are means ± SD. $*P < 0.05$, $**P < 0.001$.

of AuNPs in various serum levels. As shown in Fig. S4*B*, 20 nm AuNPs (20 μg/mL) inhibit the proliferation of A2780 cells in the presence of different concentrations of serum. These results clearly illustrate that the interactions between AuNPs and proteins is a very dynamic and complex process that warrants further investigation.

Inhibition of MAPK Activation and Intracellular Uptake Is Dependent on the Size of AuNPs. MAPK cascades play a central role in various biological processes such as meiosis, mitosis, etc. (17). Of interest is the activation (via phosphorylation) of p42/44, which when stimulated by several stimuli including GFs contributes to the increased proliferation of tumor cells (10). Furthermore, activation of this pathway is also known to induce EMT in cancer cells (19). Since AuNPs disrupt HB–GF–mediated signaling (3, 20, 21), we wanted to determine whether inhibition of AuNP-mediated proliferation could be due to an inhibition of MAPK activation in cancer cells. Our results revealed a substantial, concentration-dependent inhibition of p42/44 phosphorylation in ovarian cancer cells. While a modest inhibition was observed at lower concentration, complete abrogation of p42/44 phosphorylation was achieved when SKOV3-ip cells were treated with 20 μg of 20 nm AuNP for 48 h (Fig. 1*E*). Similar results were also observed with A2780 and OVCAR5 cells (Fig. S5 *A* and *B*). However, MAPK activation was marginally altered by 50 and 100 nm AuNPs (Fig. S5 *C* and *D*). These results suggest that 20 nm AuNPs inhibit the proliferation of ovarian cancer cells through abrogation of the MAPK signaling cascade. We also probed for two other major MAPK pathways, the Jun N-terminal kinase (Jnk), and p38 MAPK pathways (Fig. S5 *C* and *D*). These pathways are referred to as stress-activated protein kinase pathways (22). These pathways are activated due to environmental and genotoxic stress and play a key role in cellular proliferation. However, we did not observe any change in activation of either of these kinases after AuNP treatment (Fig. S5 *C* and *D*). It is likely that the efficacy of 50 and 100 nm AuNPs is limited due to the lack of GF binding to their respective surfaces. To verify the GF binding, we used an ELISA for bFGF to determine the concentrations of unbound bFGF remaining in solution after incubation with AuNPs (*SI Materials and Methods*). As shown in Fig. S5*E*, the amount of bFGF bound to the 50 and 100 nm AuNPs is less than 5%, compared with the 20 nm AuNP, which shows maximum binding. Interestingly, the antiproliferative effect of AuNPs correlated with their intracellular uptake, as quantified by Instrumental Neutron Activation Analysis (INAA). While the uptake for 5 and 20 nm AuNP was the highest, least uptake was seen for AuNPs of 50 and 100 nm size (Fig. 1*F*). The cellular uptake of the AuNPs was further confirmed using TEM (Fig. S6). We also wanted to investigate any proapoptotic property of AuNPs after treating ovarian cancer cells with various concentrations of nanoparticles for 48 h in starving conditions using DAPI staining and Annexin/propidium iodide (PI) assay, respectively. It is clear from Fig. S7 that the nuclei in the AuNP treated cells (SKOV3-ip) are intact and similar to nontreated cells, suggesting absence of cell death. These observations were further supported by the Annexin–FITC/PI assay demonstrating lack of induction of apoptosis upon AuNP treatment. These data suggest that, in addition to inhibiting the function of secreted HB–GFs, internalized AuNPs may also alter intracellular processes of the tumor cells, leading to the abrogation of the MAPK signaling. We performed all of our subsequent experiments with 20 nm AuNP as it demonstrated the highest efficacy to inhibit the proliferation and abrogate MAPK signaling of ovarian cancer cells.

AuNP Treatment Alters the Cytokine Profile in Ovarian Cancer Cells. To further understand the mechanism of AuNP-mediated inhibition of MAPK activation, we wanted to determine whether treatment with 20 nm AuNPs altered the cytokine profile in the cell lysates and conditioned media of ovarian cancer cells (Fig. 2 *A*–*D*). Treatment with AuNP substantially reduced hepatocyte GF (HGF), urokinase plasminogen activator (uPA), and bFGF levels, while the Serpin E1 level increased in the lysate of A2780 cells. However, in the conditioned media of AuNP-treated A2780 cells, transforming GF–β (TGF-β1), matrix metalloproteinase 8 (MMP 8), TNF-inducible gene 14 protein (TSG-14), and uPA levels decreased substantially, whereas the Serpin 1 level increased (Fig. 2 *A* and *C*). While the levels of bFGF, interleukin-8 (IL-8), and uPA decreased significantly in the lysate of SKOV3-ip cells after AuNP treatment, the level of Serpin E1 increased in the lysate as well as in the conditioned media. Similarly, Dipeptidyl peptidase 4 (DDP4), IL-8, PDGF, and uPA decreased significantly in the conditioned media of AuNP-treated SKOV3-ip cells, and the levels of Serpin E1 and thrombospondin-1 (THBS-1) increased (Fig. 2 *B* and *D*). Since all of these proteins are known to activate the MAPK pathway in cancer cells through various mechanisms, down-regulation of these proteins upon AuNP treatment further supports the antiproliferative effect of AuNP due to abrogation of MAPK signaling.

To determine the effect of AuNP on the expression of different GFs at the transcriptional level, quantitative RT-PCR experiments were performed for few selected targets in A2780 and SKOV3-ip cells that exhibited more than twofold change upon AuNP treatment (Fig. 2 *E* and *F*). GAPDH was used as the housekeeping gene control and the expression levels of the GFs were normalized with respect to GAPDH. It is evident from Fig. 2 *E* and *F* that uPA, bFGF, PDGF, and HGF were also transcriptionally down-regulated by AuNPs. However, TGF-β and Serpin E1 exhibits opposite effect at the transcriptional level, suggesting another level of complexity in the regulation of these proteins.

Treatment with AuNP Reverses Epithelial Plasticity of Ovarian Cancer Cells. Almost all of the cytokines discussed above have been implicated in tumor growth and metastasis in various cancers including ovarian cancer through the up-regulation of EMT

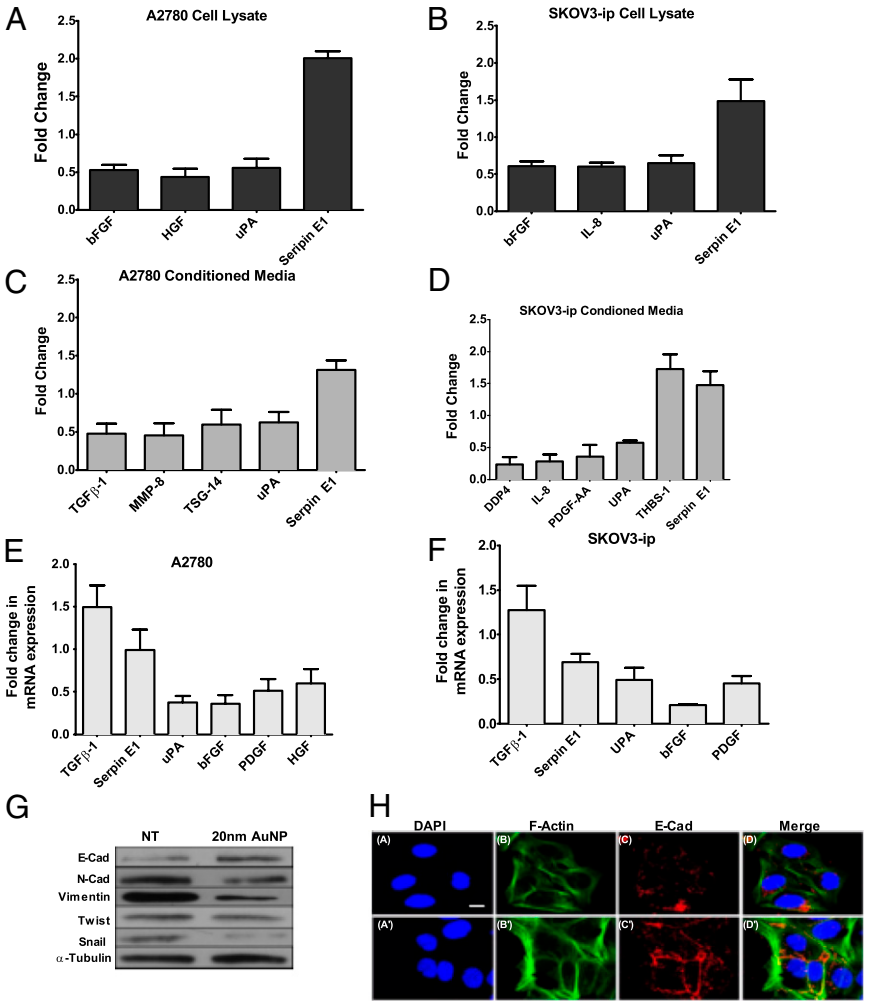

Fig. 2. Intracellular uptake of AuNPs alters the cytokine profiles as well as the EMT transition; 500 μL of lysates was tested from (*A*) A2780 and (*B*) SKOV-ip3 cell lines incubated with 20 μg of 20 nm AuNPs for 48 h. A total of 1 mL of conditioned media from (*C*) A2780 and (*D*) SKOV3-ip cell lines were incubated with 20 μg of 20 nm AuNPs for 48 h. Array signals from scanned X-ray film images were analyzed using National Institutes of Health image analysis software. Profiles of array images were created by quantifying the mean spot pixel densities using ImageJ; P values > 0.05 were not considered significant and were discarded. Results of qRT-PCR on (*E*) A2780 and (*F*) SKOV3-ip cells after 48 h incubation with 20 μg of 20 nm AuNPs. Analysis was performed on selected targets that showed a two-fold change upon 20 nm AuNP treatment from the cytokine array (*A*–*D*). (*G*) Serum-starved SKOV3-ip cells were incubated with 20 nm AuNPs (20 μg/mL) for 48 h, and the cell lysates were immunoblotted with antibodies for EMT markers. α-Tubulin was used as a loading control. Values are means ± SE. (*H*) Mesenchymal to Epithelial transition. Effect of citrate-capped AuNP treatment for 48 h on the expression and localization of E-Cad in SKOV3-ip cells. *A*–*D* show the staining for control cells and *A*′–*D*′ for nanoparticle-treated cells. *D* and *D*′ represent the merged images for DAPI (nucleus, blue), Phalloidin (F-Actin, green), and E-Cad (red). (Scale bar, 10 μm.)

pathways (epithelial plasticity) (9, 23–26). Repression of E-Cad is a hallmark of EMT and occurs through transcriptional repressors such as Vimentin, Snail, Slug, Twist, etc. (8–10). Therefore, we next determined the expression level of several EMT markers in AuNP treated versus control (nongold) samples. Incubation of 20 nm AuNPs with SKOV3-ip cells led to a significant up-regulation of E-Cad with concomitant down-regulation of its repressors Vimentin, *N*-Cad, and Snail1, thereby supporting anti-EMT function of AuNPs (Fig. 2*E*). However, the expression levels of Twist were not affected. Confocal immunofluorescence studies were performed to determine the localization of E-Cad in control and AuNP-treated SKOV3-ip cells 48 h posttreatment. Previous studies demonstrated that in epithelial cells E-Cad was predominantly localized in the plasma membrane, whereas in mesenchymal cells it was mainly localized in the perinuclear region (27–29). As shown in Fig. 2*H, Upper*, E-Cad was predominantly localized in the perinuclear regions of the control cells. However, in AuNP-treated cells, a decrease of E-Cad from the perinuclear region and a concomitant increase in the E-Cad signal at the cell membrane was noticed (Fig. 2 *H*, *Lower*). Increase in cell–cell contact was also noted through F-actin staining with fluorescently labeled phalloidin. Moreover, a total increase in the E-Cad signal intensity was also noticed in the treated cells, which corroborates with our immunoblotting data, depicting an overall increase in E-Cad in AuNP-treated cells supporting its anti-EMT function.

AuNPs Inhibit Tumor Growth in Vivo. Since AuNPs inhibited the proliferation of ovarian cancer cells and demonstrated anti-EMT function in vitro, we next sought to determine their therapeutic properties in vivo using two orthotopic mouse models of ovarian cancer. In the first model, where tumor growth was primarily localized into the ovary, we surgically implanted A2780-luciferase (luc) intrabursally into the ovaries (6–8-wk-old athymic nude female mice) and monitored the tumor growth noninvasively using bioluminescence over time (30). In the second model, we surgically implanted SKOV3-ip-luc cells intrabursally into the ovaries and monitored the tumor growth and metastasis noninvasively as stated above (*Materials and Methods*) (31). After 3 wk of 3 d/wk of i.p. injection of AuNPs, the mice ($n = 5$) were killed and tumors and metastatic nodules (see Fig. S8*A* for a representative image) were collected and measured. A substantial reduction in bioluminescence was observed in AuNP-treated mice (Fig. 3*A*) before euthanasia. The mice treated with 200 μg or 400 μg of 20 nm AuNPs had a ∼threefold reduction of tumor mass, whereas the 100 μg treatment had a ∼1.5-fold decrease compared with the PBS-treated controls (Fig. 3*B*). Likewise, analysis of gold content demonstrated that the mice treated with 200 μg and 400 μg had a three- to fourfold difference in AuNP uptake into tumors compared with the mice treated with 100 μg of 20 nm AuNPs (Fig. 3*C*). Significant uptake was also noticed in liver, with marginal uptake in the lungs and kidneys (Fig. S8*D*). However, histological analysis of the organs did not reveal any sign of inflammation or toxicity in AuNP-treated groups (Fig. S8*E*). Absence of potential toxicity of AuNPs was also reported earlier (32). Further TEM analysis confirmed the passive uptake of AuNPs into the tumors (Fig. 3*D*). To corroborate our in vitro data, we examined the effect of AuNPs on cell proliferation in vivo by Ki67 staining of the tumor samples (Fig. 3 *E* and *G*). Treatment with 200 μg of 20 nm

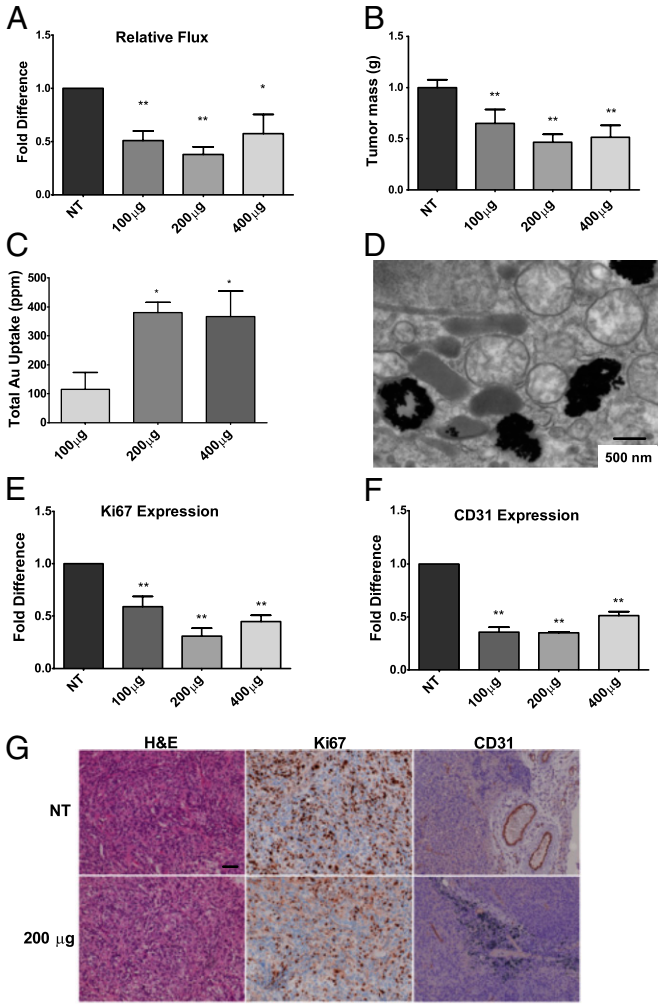

Fig. 3. AuNPs reduce tumor growth in a mouse model of ovarian cancer. A2780-luc cells were surgically implanted intrabursally into the ovaries (6–8-wk-old athymic nude female mice) and monitored the tumor growth non-invasively using bioluminescence over time. (*A*) Mice treated with AuNPs displayed a remarkable diminution in flux compared with the PBS-treated controls (NT). (*B*) Final tumor mass of the PBS-treated (NT) and AuNP-treated mice (NT). (*C*) Gold uptake into tumors using INAA analysis after necroscopy exhibiting a significant concentration-dependent increase (compared with the 100 μg treatment). (*D*) Representative TEM of tumors from mice treated with 200 μg of 20 nm AuNP postnecropspy. (*E*) Image analysis of Ki67 staining showing a notable reduction in the treated samples compared with the PBS-treated mice (NT). (*F*) AuNP treatment of mice with A2780 tumors significantly decreased microvascular density. (*G*) Representative histology of tumors from mice xenografts of A2780 cells with Ki67 expression (*Middle*) and CD31 expression (*Right*). Note in the treated sample the presence of AuNPs. Values are means ± SD. $^{**}P < 0.001$, $^{*}P < 0.05$.

AuNP showed the highest effect, with ∼70% decrease in Ki67 positive cells compared with the PBS-treated group (NT; Fig. 3*E*). Mice treated with 400 μg showed a 55% reduction in Ki67-positive cells, whereas the 100 μg–treated group showed a 40% reduction. Treatment with AuNPs also revealed a substantial decrease in number of blood vessels as determined by CD31 staining (Fig. 3 *F* and *G*), consistent with inhibitory effect of AuNPs toward HB–GF. Unlike in vitro results, a significant induction of apoptosis was also noticed in tumor tissues by TUNEL assay in the AuNP-treated group compared with control (Fig. S9).

AuNP Treatment Inhibits Tumor Growth and Metastasis in Vivo by Reversing EMT of Tumor Cells. Since AuNPs exhibited anti-EMT potential in vitro, we next sought to determine their anti-EMT efficacy in vivo reflected by the metastatic nodule formation. Since 200 μg/mouse demonstrated the highest therapeutic efficacy to inhibit tumor growth in the first model, we decided to select this dose to test the antimetastatic property of AuNP in the SKOV3-ip model. Nanoparticle (20 nm AuNP, 200 μg/mouse/d) treatment resulted in a drastic decrease in bioluminescence over the course of the study (Fig. 4*A*). AuNP-treated mice showed a substantial decrease in tumor mass (Fig. 4*B*) in comparison with sham-treated (NT) mice. Similarly, a substantial decrease in peritoneal metastasis and a reduction in number of metastatic nodule formation were observed in AuNP-treated mice compared with NT mice (Fig. 4*C*). A significant induction of apoptosis was also observed in tumor tissues of the AuNP-treated group compared with control (Fig. S9). Furthermore, Western blot analyses of the tumor samples showed a decrease in Snail and a notable increase in E-Cad upon nanoparticle treatment (Fig. 4*D*). A notable decrease in the activation of p42/44 was also observed, corroborating our in vitro data. All of these findings support the self-therapeutic anti-EMT function of AuNPs in inhibiting tumor growth and metastasis.

Discussion

EOC is one of the leading causes of morbidity among women (5). Surgical removal is generally the only option; even so, only 15–20% are suitable for surgery due to late diagnosis (33). Furthermore, despite optimal surgical debulking and meticulously designed chemotherapeutic regimens, recurrence of the disease with drug-resistant phenotype and metastatic spread is a common event (6, 33). EMT is considered to be a key mechanism that confers stem-like properties to the epithelial cancer cells, leading to metastasis and drug-resistant phenotype (9, 16). Thus, reversing the process of EMT could potentially be a unique therapeutic approach to sensitize drug-resistant cells to chemotherapeutics and to inhibit metastasis. However, down-regulation of E-Cad expression by its transcriptional repressors such as Vimentin, Snail, Slug, Twist, etc., through several redundant and independent mechanisms, poses a challenge for anti-EMT therapy (11–13). Since AuNPs can inhibit the function of a multitude of HB–GFs responsible for EMT (3, 15), it can potentially act as a multifunctional molecule to reverse epithelial plasticity, thereby inhibiting tumor growth and metastasis.

In this study, we demonstrate that AuNPs exhibit unique antitumor and anti-EMT properties that inhibit tumor growth and metastasis in two orthotopic models of ovarian cancer. The inhibition of cellular proliferation in vitro is primarily due to the abrogation of MAPK signaling, initiated by HB–GFs secreted by the cancer cells (Fig. 1). However, the proliferation of normal OSE cells is not affected, presumably because these cells have a diminished capability to secrete said GFs. The reduction of p42/44 phosphorylation is most likely due to AuNPs binding and inhibiting the function of HB–GFs as reported earlier (3, 20, 21). Since MAPK activation is a central pathway in tumor cell proliferation, AuNPs may find useful application in abrogating this pathway to inhibit tumor growth (34). Interestingly, the inhibitory effect of AuNPs is found to be correlating with their intracellular uptake pattern (Fig. 1*F*). These data suggest that, in addition to inhibiting the function of secreted HB–GFs, internalized AuNPs may also alter intracellular processes of the tumor cells, leading to the abrogation of the MAPK signaling cascade. To further understand the biological effects of internalized AuNPs, we investigated the cytokine profile in the cell lysates and conditioned media of the cancer cells after AuNP treatment.

Treatment with AuNP altered the cytokine profile in the conditioned media and cell lysates of ovarian cancer cells (Fig. 2 *A*–*D*). This treatment reduced the levels of a number of cytokines, such as HGF, TGF-β, bFGF, PDGF, uPA, etc., responsible for MAPK activation and EMT in cancer cells (35–38). For example, it has been reported that the uPA receptor (uPAR) is overexpressed in HEp3 carcinomas, promoting its rapid growth, and initiates the signaling cascade that triggers the phosphorylation of p42/44 (35, 37). This activation promotes uPA to bind to uPAR, thus creating a positive feedback loop. Likewise, a dose-dependent increase was seen in Serpin E1, which inhibits uPA. In addition,

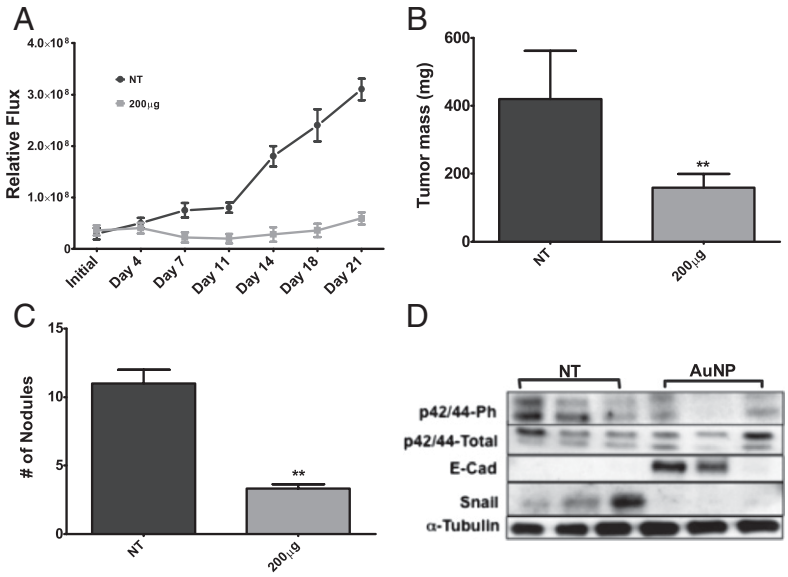

Fig. 4. AuNP treatment inhibits tumor metastasis by reversing epithelial plasticity in a mouse model of ovarian cancer. SKOV3-ip-luc cells were surgically implanted intrabursally into the ovaries (6–8-wk-old athymic nude female mice) and monitored the tumor growth noninvasively using bioluminescence over time. (*A*) Bioluminescence data show tumor growth in mice treated with 200 μg AuNPs (20 nm) considerably lessened compared with the untreated controls (NT). (*B*) Final mass of SKOV3-ip tumors in mice treated with 20 nm AuNPs or PBS treated (NT). (*C*) The number of nodules was observed to be less in the AuNP-treated group. (D) Western blot analysis of several EMT markers from the tumor tissue. α-Tubulin was used as a loading control. Values are means ± SD. $^{**}P < 0.001$, $^{*}P < 0.05$.

Serpin E1 may also have a role in regulating tumor angiogenesis and growth (36). It is also evident from Fig. 2 *E* and *F* that uPA, bFGF, PDGF, and HGF were also transcriptionally down-regulated by 20 nm AuNPs. However, TGF-β and Serpin E1 exhibited opposite effects and the transcriptional level, suggesting another level of complexity in the regulation of these proteins. It should be further noted that many of the GFs are autoregulated, such that reduction in their protein level or protein function causes reduction in their mRNA induction (39, 40). Together the results obtained from qRT-PCR and the cytokine array indicate that the AuNP treatment in the ovarian cancer cell lines does modulate the expression of the growth both at the transcriptional and translational level. Since the proteins discussed above are collectively known to induce EMT (19, 25, 41), these results suggest a possible anti-EMT function of AuNPs.

The anti-EMT function of AuNP was further supported through the enhanced expression of E-Cad upon AuNP treatment. It is well known that the down-regulation of E-Cad expression is the hallmark of epithelial plasticity (9, 41). Our data demonstrated that AuNP treatment resulted in a substantial increase in E-Cad expression with simultaneous decrease in Vimentin, Snail, and *N*-Cad expression in ovarian cancer cells, further supporting anti-EMT function of unmodified AuNPs (Fig. 2*G*). Furthermore, previous studies demonstrated that in epithelial cells E-Cad is predominantly localized in the plasma membrane, whereas in mesenchymal cells it is mainly localized in the perinuclear region (27–29). Our data showed that AuNP treatment ensued a change in the localization of E-Cad from a more perinuclear site to the cell membrane, which further supports reversal of EMT upon nanoparticle treatment (Fig. 2*H*) (42–44). Since EMT is recognized to confer drug resistance and metastatic potential to cancer cells (11–13), AuNPs may find wide applications to sensitize drug-resistant cancer cells to chemotherapeutics and to prevent metastasis.

By using human orthotopic models of ovarian cancer we are able to evaluate the antitumor and antimetastatic property of AuNPs. Treatment with AuNP significantly inhibited primary tumor growth in A2780 model (Fig. 3), wherein it significantly reduced tumor growth and formation of metastatic nodule in SKOV3-ip models (Fig. 4). It has become evident that the developmental pathways of EOC are distinct, creating variable responses to therapeutic strategies (15). Assessment of the histology of the tumor xenografts in the A2780 model yielded a significant reduction of proliferating tumor cells, as evidenced by Ki67 staining upon treatment with 20 nm AuNPs (Fig. 3*E*). Furthermore CD31 staining of the tumor tissues of AuNP-treated mice also demonstrated a reduction in the number of tumor blood vessels compared with NT mice, consistent with the inhibitory effect of AuNPs toward HB–GF (Fig. 3 *F* and *G*) (45–47). Moreover, AuNP-mediated reversal of EMT and abrogation of MAPK activation leading to inhibition of tumor growth and metastasis was further confirmed by analysis of tumor tissues by Western blot analysis (Fig. 4*D*). Western blot analysis clearly revealed an increase in E-Cad expression and decrease in p42/44-phospho and Snail in AuNP-treated tumor tissues, confirming antimetastatic property of unmodified AuNP through reversal of EMT.

Although major efforts in biomedical nanotechnology have concentrated on drug delivery and biosensing applications, biological characterization of unmodified nanoparticles still remains underinvestigated. The ability of a single self-therapeutic nanoparticle to abrogate signaling cascades of multiple GFs is distinctive and purports possible medical application. By abrogating MAPK signaling and preventing epithelial plasticity (EMT), unmodified AuNPs inhibit tumor growth and metastasis in preclinical mouse models of ovarian cancer. Our findings present a unique biological function of unmodified nanoparticles and pave the way for future investigation on the use of inorganic nanoparticles as a class of antitumor and antimetastatic agents.

Materials and Methods

Materials. Materials are provided in *SI Materials and Methods*.

Fabrication of 20 nm AuNP for Animal Model. Citrate AuNPs were prepared as previously reported (48). The synthesis process is provided in *SI Materials and Methods*.

Western Blot Analysis. Cell lysates were prepared and Western blot analyses were performed as described previously (3), and protein concentration was determined using the Protein Assay Kit (Bio-Rad) (detailed procedure is provide in *SI Materials and Methods*).

Cell Proliferation Assay. Ovarian cells (2×10^4) were seeded in 24-well plates and cultured overnight, and [^{3}H]thymidine assay was done as described previously (21) (*SI Materials and Methods*).

TEM. Transmission electron micrographs of the tumor cell lines and tumor tissues were taken on a TECNAI 12 operating at 120 kV (49) (detailed method provided in *SI Materials and Methods*).

Cellular Apoptosis Assay. The assay is described in *SI Materials and Methods*, "Measurement of Gold Content by Instrumental Neutron Activation

Analysis." Samples were analyzed by INAA as previously described (49), and details are provided in *SI Materials and Methods*.

Human Angiogenic Cytokine Array. A2780 cells were seeded at 4×10^5 in 60 mm dishes and allowed to grow under normal conditions overnight, and the assay was performed according to manufacturer's instruction (*SI Materials and Methods*).

Real-Time PCR. Total RNA was isolated from untreated and AuNP-treated A2780 and SKOV3-ip cells using RNeasy Plus Mini kit (QIAGEN). RNA was first retrotranscribed using iScript cDNA Synthesis kit (Bio-Rad), and then real-time PCR was carried out using TaqMan SYBR Green Master Mix (Applied Biosystems). The comparative C_t method was used to calculate the relative abundance of the mRNA and compared with that of GAPDH expression (50). The experiments were performed twice in triplicates. Primer sequences for qRT-PCR are provided in *SI Materials and Methods*.

Confocal Microscopy. A total of 5,000 cells of SKOV3-ip were plated per well of a four-chamber slide (Labtek) in McCoy's 5A media supplemented with 10% (vol/vol) FBS and 1% (vol/vol) antibiotics (Penicillin/Streptomycin). After incubating overnight in standard conditions, the cells were serum-starved for 24 h and treated with the citrate-capped AuNPs in serum-free McCoy's 5A media for 48 h (detailed procedure is provided in *SI Materials and Methods*). Imaging was carried on a LSM780 confocal microscope, and the images were processed using ImageJ (National Institutes of Health) software (51).

Preclinical Model of Ovarian Cancer. Before injection, tumor cells were washed twice with PBS, detached by 0.1% cold EDTA, centrifuged for 7 min, and reconstituted in HBSS (Invitrogen). Cell viability was confirmed by trypan blue exclusion. For the generation of orthotopic ovarian tumor models, 10 μL of 1×10^6 A2780 cells or SKOV3-ip cells containing luciferase (A2780-luc) were injected into the ovaries of nude mice (ages 6–8 wk) (30, 31).

Immunohistochemistry. Tumor samples were fixed in 4% paraformaldehyde and stained for H&E, Ki67, or CD31 as previously described (52). Ki67 was determined by the percentage of Ki67-positive cells in 10 high-powered fields at ×100.

Statistical Analysis. All values are expressed as means ± SD. Statistical significance was determined using two-sided Student *t* test. For animal experiments, five mice were assigned per treatment group. To judge the necessary sample size for proposed experiments, we considered a one-way ANOVA model using Kruskal–Wallis. $*P < 0.05$ and $**P < 0.001$ were considered significant.

ACKNOWLEDGMENTS. This research was supported by National Institutes of Health Grant CA135011 and CA136494 (to P.M.) and CA157481(to R.B.).

1. Arvizo RR, et al. (2012) Intrinsic therapeutic applications of noble metal nanoparticles: Past, present and future. *Chem Soc Rev* 41(7):2943–2970.
2. Patra CR, et al. (2008) Targeted delivery of gemcitabine to pancreatic adenocarcinoma using cetuximab as a targeting agent. *Cancer Res* 68(6):1970–1978.
3. Arvizo RR, et al. (2011) Mechanism of anti-angiogenic property of gold nanoparticles: Role of nanoparticle size and surface charge. *Nanomedicine* 7(5):580–587.
4. Jain RK (2005) Normalization of tumor vasculature: An emerging concept in anti-angiogenic therapy. *Science* 307(5706):58–62.
5. Jemal A, Siegel R, Xu J, Ward E (2010) Cancer statistics, 2010. *CA Cancer J Clin* 60(5):277–300.
6. Yap TA, Carden CP, Kaye SB (2009) Beyond chemotherapy: Targeted therapies in ovarian cancer. *Nat Rev Cancer* 9(3):167–181.
7. Cooke VG, et al. (2012) Pericyte depletion results in hypoxia-associated epithelial-to-mesenchymal transition and metastasis mediated by met signaling pathway. *Cancer Cell* 21(1):66–81.
8. Thiery JP, Acloque H, Huang RYJ, Nieto MA (2009) Epithelial-mesenchymal transitions in development and disease. *Cell* 139(5):871–890.
9. Lee JM, Dedhar S, Kalluri R, Thompson EW (2006) The epithelial-mesenchymal transition: New insights in signaling, development, and disease. *J Cell Biol* 172(7):973–981.
10. Nauseef JT, Henry MD (2011) Epithelial-to-mesenchymal transition in prostate cancer: Paradigm or puzzle? *Nat Rev Urol* 8(8):428–439.
11. Kajiyama H, et al. (2007) Chemoresistance to paclitaxel induces epithelial-mesenchymal transition and enhances metastatic potential for epithelial ovarian carcinoma cells. *Int J Oncol* 31(2):277–283.
12. Singh A, Settleman J (2010) EMT, cancer stem cells and drug resistance: An emerging axis of evil in the war on cancer. *Oncogene* 29(34):4741–4751.
13. Voulgari A, Pintzas A (2009) Epithelial–mesenchymal transition in cancer metastasis: Mechanisms, markers and strategies to overcome drug resistance in the clinic. *Biochim Biophys Acta Rev Can* 1796(2):75–90.
14. Bhattacharya R, Mukherjee P (2008) Biological properties of "naked" metal nanoparticles. *Adv Drug Deliv Rev* 60(11):1289–1306.
15. Landen CN, Jr., Birrer MJ, Sood AK (2008) Early events in the pathogenesis of epithelial ovarian cancer. *J Clin Oncol* 26(6):995–1005.
16. Tiwari N, Gheldof A, Tatari M, Christofori G (2012) EMT as the ultimate survival mechanism of cancer cells. *Semin Cancer Biol* 22(3):194–207.
17. Cordenonsi M, et al. (2007) Integration of TGF-beta and Ras/MAPK signaling through p53 phosphorylation. *Science* 315(5813):840–843.
18. Bhattacharya R, et al. (2008) Role of hedgehog signaling in ovarian cancer. *Clin Cancer Res* 14(23):7659–7666.
19. Grotegut S, von Schweinitz D, Christofori G, Lehembre F (2006) Hepatocyte growth factor induces cell scattering through MAPK/Egr-1-mediated upregulation of Snail. *EMBO J* 25(15):3534–3545.
20. Bhattacharya R, et al. (2004) Gold nanoparticles inhibit VEGF165-induced proliferation of HUVEC cells. *Nano Lett* 4(12):2479–2481.
21. Mukherjee P, et al. (2005) Antiangiogenic properties of gold nanoparticles. *Clin Cancer Res* 11(9):3530–3534.
22. Wagner EF, Nebreda AR (2009) Signal integration by JNK and p38 MAPK pathways in cancer development. *Nat Rev Cancer* 9(8):537–549.
23. Dumont N, Arteaga CL (2003) Targeting the TGF beta signaling network in human neoplasia. *Cancer Cell* 3(6):531–536.
24. Eichhorn PJA, et al. (2012) USP15 stabilizes TGF-β receptor I and promotes oncogenesis through the activation of TGF-β signaling in glioblastoma. *Nat Med* 18(3):429–435.
25. Massagué J (2008) TGFbeta in cancer. *Cell* 134(2):215–230.
26. Siegel PM, Massagué J (2003) Cytostatic and apoptotic actions of TGF-β in homeostasis and cancer. *Nat Rev Cancer* 3(11):807–821.
27. Larue L, Bellacosa A (2005) Epithelial-mesenchymal transition in development and cancer: Role of phosphatidylinositol 3′ kinase/AKT pathways. *Oncogene* 24(50):7443–7454.
28. Palacios F, Tushir JS, Fujita Y, D'Souza-Schorey C (2005) Lysosomal targeting of E-cadherin: A unique mechanism for the down-regulation of cell-cell adhesion during epithelial to mesenchymal transitions. *Mol Cell Biol* 25(1):389–402.
29. Thiery JP, Sleeman JP (2006) Complex networks orchestrate epithelial-mesenchymal transitions. *Nat Rev Mol Cell Biol* 7(2):131–142.
30. Bao R, et al. (2002) Activation of cancer-specific gene expression by the survivin promoter. *J Natl Cancer Inst* 94(7):522–528.
31. Shao M, et al. (2009) Epithelial-to-mesenchymal transition and ovarian tumor progression induced by tissue transglutaminase. *Cancer Res* 69(24):9192–9201.
32. Hainfeld JF, Slatkin DN, Focella TM, Smilowitz HM (2006) Gold nanoparticles: A new X-ray contrast agent. *Br J Radiol* 79(939):248–253.
33. Hennessy BT, Coleman RL, Markman M (2009) Ovarian cancer. *Lancet* 374(9698):1371–1382.
34. Solit DB, et al. (2006) BRAF mutation predicts sensitivity to MEK inhibition. *Nature* 439(7074):358–362.
35. Aguirre-Ghiso JA, Estrada Y, Liu D, Ossowski L (2003) ERK(MAPK) activity as a determinant of tumor growth and dormancy; regulation by p38(SAPK). *Cancer Res* 63(7):1684–1695.
36. Aguirre Ghiso JA (2002) Inhibition of FAK signaling activated by urokinase receptor induces dormancy in human carcinoma cells in vivo. *Oncogene* 21(16):2513–2524.
37. Liu D, Aguirre Ghiso J, Estrada Y, Ossowski L (2002) EGFR is a transducer of the urokinase receptor initiated signal that is required for in vivo growth of a human carcinoma. *Cancer Cell* 1(5):445–457.
38. Mahner S, et al. (2010) TIMP-1 and VEGF-165 serum concentration during first-line therapy of ovarian cancer patients. *BMC Cancer* 10(1):139.
39. Bartel DP (2009) MicroRNAs: Target recognition and regulatory functions. *Cell* 136(2):215–233.
40. Filipowicz W, Bhattacharyya SN, Sonenberg N (2008) Mechanisms of post-transcriptional regulation by microRNAs: Are the answers in sight? *Nat Rev Genet* 9(2):102–114.
41. Xie L, et al. (2004) Activation of the Erk pathway is required for TGF-β1-induced EMT in vitro. *Neoplasia* 6(5):603–610.
42. Auersperg N, et al. (1999) E-cadherin induces mesenchymal-to-epithelial transition in human ovarian surface epithelium. *Proc Natl Acad Sci USA* 96(11):6249–6254.
43. Spencer HL, et al. (2007) E-cadherin inhibits cell surface localization of the pro-migratory 5T4 oncofetal antigen in mouse embryonic stem cells. *Mol Biol Cell* 18(8):2838–2851.
44. Tiraby C, Hazen BC, Gantner ML, Kralli A (2011) Estrogen-related receptor gamma promotes mesenchymal-to-epithelial transition and suppresses breast tumor growth. *Cancer Res* 71(7):2518–2528.
45. Bamberger ES, Perrett CW (2002) Angiogenesis in epithelian ovarian cancer. *Mol Pathol* 55(6):348–359.
46. Ramakrishnan S, Subramanian IV, Yokoyama Y, Geller M (2005) Angiogenesis in normal and neoplastic ovaries. *Angiogenesis* 8(2):169–182.
47. Schumacher JJ, et al. (2007) Modulation of angiogenic phenotype alters tumorigenicity in rat ovarian epithelial cells. *Cancer Res* 67(8):3683–3690.
48. Grabar K, Freeman R, Hommer M, Natan M (1995) Preparation and characterization of Au colloid monolayers. *Anal Chem* 67(4):735–743.
49. Arvizo RR, et al. (2010) Effect of nanoparticle surface charge at the plasma membrane and beyond. *Nano Lett* 10(7):2543–2548.
50. Schmittgen TDLK, Livak KJ (2008) Analyzing real-time PCR data by the comparative C(T) method. *Nat Protoc* 3(6):1101–1108.
51. Bhattacharyya S, Bhattacharya R, Curley S, McNiven MA, Mukherjee P (2010) Nanoconjugation modulates the trafficking and mechanism of antibody induced receptor endocytosis. *Proc Natl Acad Sci USA* 107(33):14541–14546.
52. Olive KP, et al. (2009) Inhibition of Hedgehog signaling enhances delivery of chemotherapy in a mouse model of pancreatic cancer. *Science* 324(5933):1457–1461.